coatings

MDPI

Article

Fabrication of Pyramid/Porous Composite Structures for Mitigating Surface Optical Losses in Perovskite Solar Cells

Xiaohao Shi [1,†], Zhou Jiang [1,†], Yuxuan Du [1,†], Chen Wang [1], Bin Luo [1], Xiaodan Wang [2] and Xiangqian Shen [1,3,*]

[1] Xinjiang Key Laboratory of Solid State Physics and Devices, School of Physical Science and Technology, Xinjiang University, Urumqi 830046, China
[2] Department Interface Design, Helmholtz-Zentrum Berlin für Materialien und Energie GmbH (HZB), Albert-Einstein-Str. 15, 12489 Berlin, Germany
[3] State Key Laboratory of Metal Matrix Composites, Shanghai Jiao Tong University, Shanghai 200240, China
* Correspondence: sxqlyq@sjtu.edu.cn
† These authors contributed equally to this work.

Abstract: Surface optical losses represent one of the critical factors limiting the photogenerated current density and power conversion efficiency (PCE) of perovskite solar cells (PSCs). To address this issue, this paper introduces a pyramid/porous composite structure on the light-facing surface of PSCs. The pyramids and porous structures are obtained on silicon surfaces via alkaline wet etching and metal-assisted chemical etching, respectively, and then replicated onto the cell surface using nanoimprint technology. The research findings indicate that the micrometer-scale pyramids induce multiple refractions of incident light, enhancing the probability of photons entering the interior of the cell. Moreover, the nanoscale porous structures on the pyramid mitigate the refractive index difference between air and the pyramid material, thereby reducing reflection losses for single-incident light. For the optimized pyramid/porous structure, a reduction in surface reflectivity from 40.3% to 5.1% is observed on silicon. Benefiting from the suppression of surface reflection losses by the pyramid/porous structure, the response spectrum of the PSCs is significantly improved. Consequently, the photogenerated current density of the device increases from 21.62 to 23.86 mA cm^{-2}, with a relative enhancement in PCE by 9.5%.

Keywords: perovskite solar cells; pyramid/porous composite structure; reflection loss reduction; optical regulation; efficiency enhancement

Academic Editor: Vaidotas Kazukauskas

Received: 5 January 2025
Revised: 14 February 2025
Accepted: 18 February 2025
Published: 25 February 2025

Citation: Shi, X.; Jiang, Z.; Du, Y.; Wang, C.; Luo, B.; Wang, X.; Shen, X. Fabrication of Pyramid/Porous Composite Structures for Mitigating Surface Optical Losses in Perovskite Solar Cells. *Coatings* **2025**, *15*, 273. https://doi.org/10.3390/coatings15030273

1. Introduction

Organic–inorganic hybrid perovskite solar cells (PSCs) have garnered intense attention from numerous researchers upon their emergence, due to their distinctive optoelectronic properties such as high absorption coefficients in the visible and near-infrared regions, long carrier lifetimes, high mobilities, tunable band gaps, and high defect tolerance [1–3]. Furthermore, these cells boast advantages of low cost, abundant raw materials, and solution processability, positioning them as key competitors to break the monopoly of traditional silicon-based solar cells in the photovoltaic market. Consequently, they have increasingly gained traction in the industrial sector [4,5]. Through the diligent efforts of scholars worldwide, the PCE of PSCs has soared from an initial 3.8% to a remarkable ~26%, gradually approaching the Shockley–Queisser (S–Q) limit for single-junction cells [6,7]. Meanwhile, reported module efficiencies have surpassed 20%, presenting a highly attractive commercial outlook [8].

Mechanistically, PSCs function as photoelectric conversion devices. Enhancing their PCE hinges on enabling the active layer to absorb sufficient photons while ensuring that

photogenerated carriers are effectively collected by the external electrodes, a process involving both optical and electrical aspects. On the electrical front, non-radiative recombination induced by defects is a significant factor leading to carrier losses, which can be regulated through solvent engineering, compositional engineering, interface modification, and crystallization kinetics [9,10]. In terms of optics, losses primarily encompass three components [11,12]: (1) reflection losses at interfaces (surface/interfaces) due to refractive index mismatches among the various thin-film materials stacked in PSCs; (2) parasitic absorption losses in non-responsive materials such as transparent electrodes and charge transport layers; and (3) non-absorption (transmission) losses of photons with energies below the bandgap of the active layer. Among these, the latter two optical losses are predominantly determined by the cell's configuration and material composition. Therefore, the core of optical manipulation lies in reducing the optical losses at the cell surface.

To mitigate these losses, various strategies have been employed, with anti-reflection coatings (ARCs) being a prominent approach [13]. ARCs utilize the principle of destructive interference between incident light and reflected light to minimize reflection. By carefully selecting the refractive index and thickness of the coating material, the reflected waves from the air–coating interface and the coating–substrate interface can interfere destructively, effectively canceling each other out and reducing reflection. One major limitation is that these coatings are highly wavelength-dependent. They are typically optimized for a specific wavelength or a narrow range of wavelengths, meaning they may not perform well across a broad spectrum. An alternative approach involves the design of gradient refractive index (GRIN) structures [14], which gradually transition the refractive index from the PSC surface to the surrounding medium. This gradient reduces the abrupt change in the refractive index that leads to reflection, thus enhancing light coupling into the PSC. GRIN structures offer the advantage of being more adaptable to different wavelengths and incident angles, potentially broadening the spectral and angular acceptance of PSCs. However, implementing GRIN structures in PSCs faces challenges such as precise control over the refractive index gradient during fabrication, which requires advanced and often complex manufacturing techniques. Additionally, maintaining the structural integrity and stability of GRIN layers under operational conditions, especially in the presence of moisture and temperature fluctuations, remains a significant hurdle.

In recent years, various micro- and nanostructured designs have been proposed. Compared to ARCs and GRIN, micro- and nano-photonic structures offer greater flexibility and superior optical enhancement due to their customizable morphologies and feature sizes. For instance, Jae Su Yu and colleagues employed soft lithography to create micron-sized inverted pyramid structures on the surface of PSCs, significantly reducing reflection losses and increasing the average haze of transmitted light, thereby leading to substantial improvements in photocurrent and PCE [15]. Peer et al. fabricated a layer of microlenses of specific sizes on the illuminated surface of the cell through imprinting, a design that mitigated the cavity effect in planar structures and enhanced the light trapping effect for photons near the bandgap [16]. More recently, Ji Seong Choi and team demonstrated the promising potential of moth-eye bio-inspired structures in optical manipulation for perovskite solar cells. They developed an ultra-thin moth-eye structure on a low-refractive-index (n = 1.34) perfluoropolyether (PFPE) material, which exhibits excellent light transmittance and mechanical flexibility. Both rigid and flexible cells based on this coating achieved the highest short-circuit current densities (J_{SC}) among their respective peer groups [17]. Regarding the primary challenges associated with the application of micro- and nano-photonic structures in PSCs, several issues stand out. Notably, the preparation costs can be significant, as the fabrication processes often involve sophisticated techniques and materials. Further-

more, the complexity of these processes can hinder scalability and reproducibility, posing additional barriers to widespread adoption.

In this paper, a pyramid/porous composite structure is designed. The pyramids and pores are obtained on the silicon surface through alkaline wet etching and metal-assisted chemical etching, respectively [18,19]. Subsequently, the pyramid/porous structure on the silicon surface is replicated onto the light-facing side of the PSCs using nanoimprint lithography [20–22]. Here, the pyramids possess micrometer-scale dimensions, with an included angle of 54.74° between their faces, which facilitates multiple refractions of incident light among the pyramids, thereby enhancing the probability of light entering the interior of the cell. Meanwhile, the porous structure on the pyramid faces mitigates the refractive index difference between air and the pyramid material, consequently reducing the reflection loss for a single incidence. Through the modulation of the pyramid/porous composite structure, the reflection loss on the surface of the PSCs is significantly suppressed, leading to a notable improvement in the corresponding photoelectric response performance of the device. Compared to other micro- and nano-photonic structures used for anti-reflection, the pyramids and porous structures presented herein do not require expensive templates for their fabrication. Additionally, this composite structure can be replicated multiple times using itself as a template, further reducing costs and simplifying the production process.

2. Experimental Section

The preparation process of the pyramid/porous composite structure is illustrated in Figure 1. First, a planar monocrystalline silicon substrate is prepared and subsequently etched to create micron-scale pyramids using alkaline wet etching. Following this, a metal-assisted chemical etching step is employed to generate nano-scaled pores on the pyramid surfaces, resulting in the desired pyramid/porous composite structure. Finally, this composite structure is replicated onto the illuminated surface of PSCs through nanoimprint lithography. Below is a detailed description of each step:

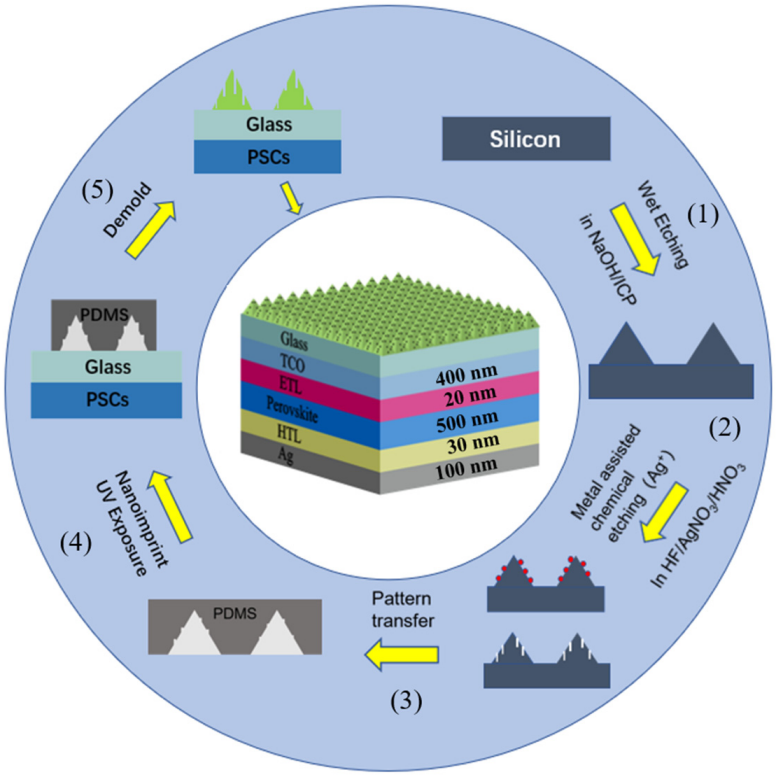

Figure 1. Schematic illustration of the preparation process of the pyramid/porous composite structure and its position within the PSC.

(1) Preparation of Micrometer-Scale Pyramid Structures. Initially, the silicon wafers were sequentially immersed in deionized water, hydrogen peroxide (H_2O_2), ethanol, and again in deionized water for ultrasonic cleaning for 10 min each step. This process removes oils, greases, and metallic ions from the silicon surface. Following the ultrasonic cleaning, the wafers were then dried using nitrogen gas to eliminate any residual moisture. Subsequently, the cleaned silicon wafers were placed into a well-prepared 5% HF (Hydrofluoric Acid) solution for etching for 5 min. This step is crucial to strip off the SiO_2 oxide layer that forms naturally on the silicon surface due to prolonged exposure to air. The wafers, now devoid of the native oxide layer, were introduced into a solution of NaOH (Sodium Hydroxide) that had been appropriately formulated (step 1). Here, the solvent for NaOH is water. To this NaOH solution, a specified amount of isopropanol was added, followed by the incorporation of additives: sodium lignosulfonate (SL), cyclodextrin, and sodium carbonate (Na_2CO_3). The mixture containing the silicon wafers was then subjected to water bath heating to facilitate the etching process, which resulted in the formation of pyramid structures on the silicon surface. The textured silicon wafers were once again immersed in a freshly prepared 5% HF solution for an additional 5 min to eliminate any impurities or residual etchants from the surface. To further purify the surface, the wafers were rinsed in deionized water for 2 min to neutralize and remove any trace amounts of HF.

(2) Formation of Nanoporous Structures on Pyramids. To create the desired nanoporous structures on the previously etched silicon templates with micrometer-sized "pyramid" structures, a second etching step was performed using Ag ion-assisted metal-catalyzed chemical etching. A mixed solution containing silver nitrate ($AgNO_3$), HF, H_2O_2, and nitric acid (HNO_3) was prepared in a specific proportion. The silicon templates with "pyramid" structures were then immersed into this solution and heated in a water bath at a controlled temperature for a certain duration (step 2). After the etching process, the samples were retrieved. To remove any potential residual products from the etching process, the prepared samples underwent a cleaning procedure. They were soaked in a solution of deionized water and diluted HNO_3 for a period of time, followed by rinsing extensively with deionized water. It is recommended to rinse the samples multiple times with deionized water to ensure thorough removal of any residuals. Finally, the samples were dried using nitrogen gas.

(3) Replication of Pyramid/Nanoporous Structure onto Perovskite Solar Cell Surface. First, the solution of polydimethylsiloxane (PDMS) and its curing agent was meticulously mixed in a strict ratio of 10:1 using a syringe and poured into a glass bottle. This mixture was then placed in a mixing instrument for thorough agitation for 20 min to ensure complete integration of the sol and curing agent. Subsequently, the glass bottle was transferred into a vacuum chamber to eliminate air bubbles, thereby preventing stress concentration within the material. Next, a silicon wafer etched with pyramid/porous structures was mounted onto a spin coater. The pre-mixed PDMS solution was dispensed onto the silicon wafer using a syringe, and then evenly spread across the surface through spin coating at a speed of 2000 rpm. To achieve a desired thickness of ~5 μm for the PDMS soft template, the process of spin coating followed by curing was repeated multiple times. Following the final cure, the template was carefully demolded from the silicon wafer (step 3). The resultant PDMS soft template was then positioned and secured within the upper imprint chamber. Meanwhile, a layer of imprint resin was coated onto the surface of the PSC, which was subsequently fixed in the lower imprint chamber (step 4). The nanoimprint equipment was operated to adjust the imprint parameters, initiating the imprinting process. After successful imprinting, ultraviolet (UV) curing was performed to solidify the resin, followed by demolding to reveal the pyramid/porous structures on the surface of the PSC (step 5).

(4) Preparation of PSCs. The structural schematic of the PSC is illustrated in Figure 1. Here, the perovskite employed a FAMA binary mixed cation system, with its conduction band minimum (CBM) and valence band maximum (VBM) positioned at −3.85 eV and −5.4 eV, respectively. The electron transport layer (ETL) and hole transport layer (HTL) consisted of SnO_2 and PTAA, which have CBM and VBM values of −4.4 eV and −5.2 eV. The perovskite layer absorbed photons, generating electron–hole pairs. These electrons and holes were subsequently extracted by the ETL and HTL, respectively, and finally collected by the electrodes at both ends. The detailed fabrication process of the PSC is as follows: The etched fluorine doped tin oxide (FTO, 13 Ω/Y) glass was sequentially placed in detergent, deionized water, ethanol, and then isopropanol, with each step involving ultrasonic cleaning for 15 min. Following this, the glass was immersed in isopropanol. Residual isopropanol on the substrate was removed by nitrogen gas blowing with a drying treatment. Subsequently, the substrate was subjected to a 20 min treatment using a UV ozone cleaner to eliminate surface organic residues. A dispersion of SnO_2 nanoparticles was diluted with deionized water in a volume ratio of 1:8.5 (v:v). This diluted solution was then deposited onto the FTO side of the substrate using a static spin-coating method at a speed of 3000 rpm. Following deposition, the sample was annealed on a hotplate at 150 °C for 30 min. The sample was transferred into a nitrogen-filled glovebox. A 1.5 Mol solution of PbI_2 in a DMF/DMSO mixture (9:1 ratio) was spin-coated onto the electron transport layer using a static spin-coating method with a rotation speed of 1500 rpm for 40 s. This was followed by annealing on a hotplate at 80 °C for 2 min. After the sample cooled down, a mixed solution of FAI/MAI/MACl in isopropanol (concentration of 90:9:9 mg mL^{-1}) was dynamically spin-coated onto the PbI_2 film at a speed of 1500 rpm for 30 s. During the final 10 s of spin coating, 150 μL of chlorobenzene was dripped onto the film. The sample was then annealed on a hotplate at 100 °C for 10 min. PTAA was dissolved in a mixture of 1 mL of toluene and 4 μL of tBP to form a solution. This PTAA solution was then dynamically spin-coated onto the substrate at a speed of 3000 rpm, resulting in the formation of the hole transport layer. Finally, the sample was placed in a thermal evaporation coating machine to deposit a 100 nm thick silver electrode. The active area of the PSCs, which is determined by the aperture size of the shadow mask during electrode deposition, measured 0.09 cm^2.

(5) Characterization. The morphologies of pyramid/nanoporous structures were observed using Field-emission Scanning Electron Microscopy (FESEM; FEI Nova NanoSEM 450, FEI, Lincoln, NU, USA). During the observation using FESEM, the accelerating voltage was set to 5 KeV, and the working distance was maintained at 10 mm. The reflection and absorption spectrum were characterized using a UV/visible/near-infrared spectrophotometer (Lambda 950, Perkin Elmer, Hopkinton, MA, USA). The PCE of the PSCs was assessed using a solar simulator (SolarIV-150A, Zolix Instruments, Beijing, China). This system allowed for the precise measurement of the cells' power output under standardized illumination conditions, mimicking the AM1.5G solar spectrum. The external quantum efficiency (EQE) of the devices was evaluated using a Quantum Efficiency Measurement System (7-SCSPEC3, Zolix Optoelectronics, Beijing, China). All the measurements were conducted under controlled environmental conditions to minimize variations due to temperature and spectral mismatches.

3. Results and Discussion

Firstly, the impact of various etching conditions on the morphology of pyramids and the corresponding reflectivity of silicon surfaces was investigated. When monocrystalline silicon is placed in an alkaline solution containing NaOH plus isopropyl alcohol, a chemical reaction occurs, as described by the following equations:

$$Si + 6OH^- \rightarrow SiO_3^{2-} + H_2O + 4e^- \quad (1)$$

$$4H^+ + 4e^- \rightarrow 2H_2 \uparrow \quad (2)$$

The overall reaction can be summarized as follows:

$$Si + 2OH^- + H_2O = SiO_3^{2-} + 2H_2 \uparrow \quad (3)$$

Crystalline silicon possesses three distinct crystallographic orientations: (100), (110), and (111). Due to the varying number of dangling bonds accompanying the silicon atoms on each crystallographic plane, the reaction rates of monocrystalline silicon in alkaline solutions differ across these planes, a phenomenon known as anisotropic etching. In a solution of a certain alkalinity concentration, the etching rate of the (111) plane is slower than that of the (100) plane, leading to the formation of unique "pyramid" structures during the etching process. To ensure minimal attachment of H_2 and silicates produced by the reaction on the silicon surface during pyramid formation, additional additives are incorporated. These additives are formulated by mixing sodium lignosulfonate (SL), cyclodextrin, and sodium carbonate (Na_2CO_3) in specific proportions of 0.4 wt%, 5 wt%, and 3 wt%, respectively. These additives prevent localized reactions from proceeding too slowly, thereby avoiding inconsistencies in pyramid size. Prior to creating a pyramid layer of a certain thickness on the silicon substrate, preprocessing steps are essential to prevent the etching solution from penetrating into the silicon substrate and causing irreversible damage. With the addition of these additives, the nucleation process can be effectively controlled, resulting in a more uniform distribution of pyramid-shaped structures. In general, the morphology, size, and distribution of the pyramids are influenced by the concentration of NaOH, the concentration of additives, and the etching duration.

Figure 2 presents the SEM images of silicon surfaces corresponding to different etching times, with fixed concentrations of NaOH and additives. At an etching duration of 10 min, the pyramids are still in the "nucleation point" stage, where numerous "pyramid tips" exist unevenly distributed on the silicon template surface. Only a few fully formed pyramids are observed, and some areas remain uncovered by these tips, as depicted in Figure 2(a1,a2). When the etching time reaches 20 min, many unevenly distributed "small pyramids" begin to emerge on the silicon template surface, with a small number of areas still uncovered by these small pyramids. At an etching duration of 30 min, a large number of pyramids on the silicon template surface start to become complete, and their distribution becomes more uniform, with nearly all areas now covered by pyramids. As shown in Figure 2(b1,b2), when the etching time is 40 min, well-formed pyramids are uniformly distributed across the silicon template surface, and stacking overlay begins to appear, with almost no gaps between the pyramids. As illustrated in Figure 2(c1,c2), when the etching duration reaches 50 min, the pyramids on the silicon template surface start to "collapse", with some pyramids gradually disappearing and certain areas showing signs of "over-etching".

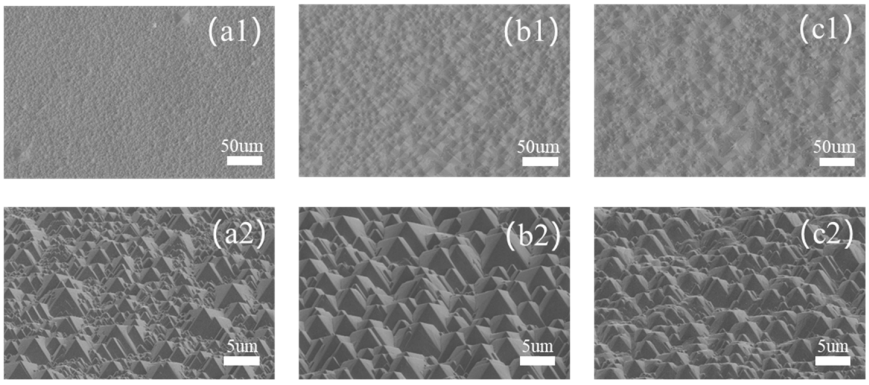

Figure 2. Variation in pyramid morphology on silicon surface with etching time. (**a1**) 20 min, (**b1**) 40 min, (**c1**) 50 min. (**a2**), (**b2**), and (**c2**) are the partially enlarged views of (**a1**), (**b1**), and (**c1**), respectively.

To further investigate the impact of the etching duration on the pyramid structure, the surface reflectivity of the aforementioned samples was measured and compared with that of an unetched sample (flat silicon), as illustrated in Figure 3. Considering the uneven energy distribution across various wavelengths in the solar spectrum, the weighted average reflectivity R_{av} was adopted as the evaluation criterion, calculated using the following formula:

$$R_{av} = \frac{\int_{\lambda_{min}}^{\lambda_{max}} S(\lambda)R(\lambda)d\lambda}{\int_{\lambda_{min}}^{\lambda_{max}} S(\lambda)d\lambda} \quad (4)$$

where $S(\lambda)$ denotes the standard AM1.5 solar spectrum, $R(\lambda)$ represents the reflectance spectrum obtained from the measurements, and λ_{min} and λ_{max} are the minimum and maximum response wavelengths of the cell devices, respectively. As shown in Figure 3, the planar silicon exhibits a reflectivity of approximately 40% in the visible region, yielding a calculated R_{av} of 40.3%. With increasing etching duration, a significant decrease in the reflectance spectrum is observed, reaching its lowest point at 40 min, where R_{av} is 14%. This phenomenon can be explained by the theory of multiple reflections. Since the size of the pyramids is on the micrometer scale, much larger than the wavelength of the incident light, the reflection of light on the pyramid faces obeys the law of reflection. Unlike planar silicon, incident light reflected by one pyramid face does not directly lose energy but instead strikes another pyramid face, providing multiple opportunities for the light to enter the silicon wafer. If the reflection coefficient for a single incidence is R, after n incidences, the reflection coefficient is reduced to R^n. Extensive research has shown that the angle between adjacent faces of pyramids etched using NaOH alkaline solution is 54.74°, ensuring that most incident light undergoes two or more reflections, thus reducing the reflectivity below 16%. As the etching duration continues to increase, the reflectivity begins to rise due to "over-etching" that results in the disappearance of some pyramids, consequently reducing the number of incident light rays undergoing multiple reflections. Therefore, it can be concluded that the overall morphology of the pyramids is optimal when the etching duration is 40 min. Similarly, the effects of the NaOH concentration and additive concentration on pyramid etching were studied. The R_{av} values calculated under different conditions are presented in Figure 4. It can be observed that the optimal concentrations of NaOH and the additive are 3% and 5%, respectively.

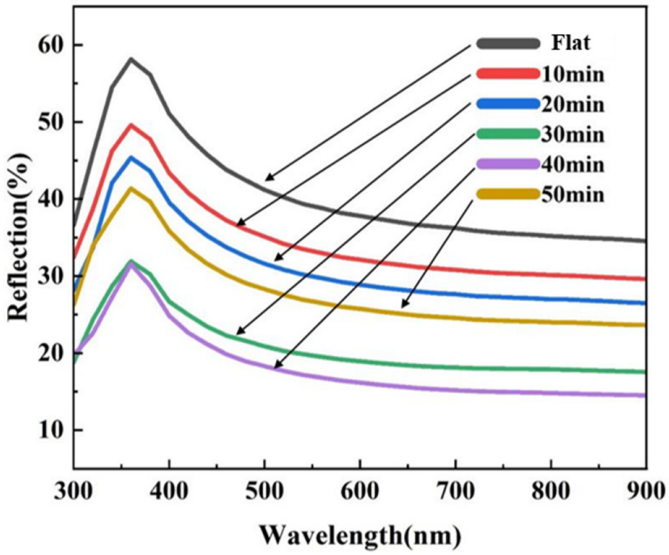

Figure 3. Relationship between the reflection spectrum of the silicon surface and the etching time.

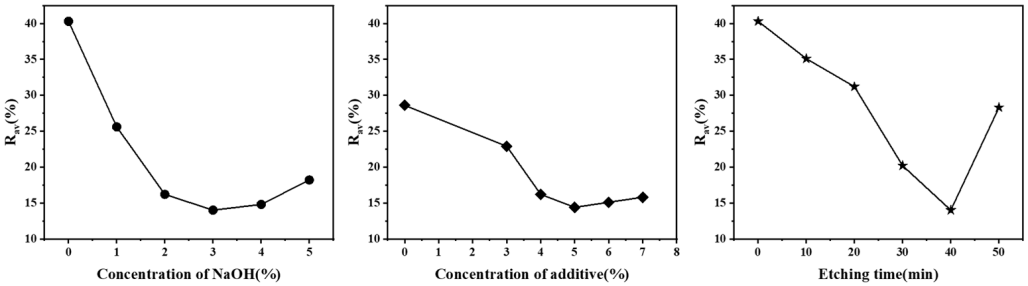

Figure 4. Relationship between the weighted average reflectance of silicon surface and various etching conditions.

The silicon samples with etched "pyramid" structures underwent a second etch using Ag ion-assisted metal-catalyzed chemical etching, resulting in the formation of nanoscale porous structures on the surfaces of the "pyramid" structures, thereby yielding a pyramid/porous composite structure. During the etching process in a mixed $AgNO_3$/HF solution, the reaction equation is as follows:

$$\text{cathode e reaction: } Ag^+ + e^- \rightarrow Ag \quad (5)$$

$$\text{anodic reaction: } Si + 6F^- \rightarrow SiF_6^- + 4e^- \quad (6)$$

$$\text{total reaction: } 4Ag^- + Si + 6F^- \rightarrow 4Ag + SiF_6^- \quad (7)$$

During the second etching step, variations in etching conditions also influenced the structural morphology, with the most notable impact observed from changes in the $AgNO_3$ concentration. To this end, the proportions of the mixed HNO_3, HF, and H_2O_2 solution (HNO_3:HF:H_2O_2 = 1:6:3) and the reaction temperature (30 °C) were kept constant. With the $AgNO_3$ concentrations varying between 0 and 0.06 Mol, the SEM images of the silicon surfaces are presented in Figure 5. These images reveal that the pyramid surfaces etched by metal-catalyzed chemical etching exhibited irregularly distributed pores with diameters of tens of nanometers, transforming the surfaces from smooth to rough. As shown in Figure 5(a1,a2), when the $AgNO_3$ concentration was low, the number of pores was relatively small, and there were significant diameter differences among the pores, indicating that the pyramid surface was not fully etched at this stage. As the $AgNO_3$ concentration increased, the etching of the pyramid faces became more thorough.

Figure 5(b1,b2) demonstrates that when the $AgNO_3$ concentration reached 0.05 Mol, the pyramids were nearly completely etched, with their surfaces uniformly covered by pores of varying sizes. With further increases in the $AgNO_3$ concentration, some pore walls were completely penetrated, connecting adjacent pores, and notable "collapsed areas" could be observed on the pyramid surfaces, as illustrated in Figure 5(c1,c2). Figure 6 presents the reflectance spectra of the pyramid/porous composite structures obtained after the second etching. It is evident that compared to the single pyramid structure (0 min), the reflectance of the composite structure with pores further decreased. When the $AgNO_3$ concentration was 0.05 Mol, the overall reflectance spectrum was the lowest, with R_{av} at 5.1%. Here, the introduction of the porous structure reduced the refractive index difference between air and silicon, thereby decreasing the reflectance upon a single incidence of light. In essence, the porous structure functioned as an anti-reflective coating.

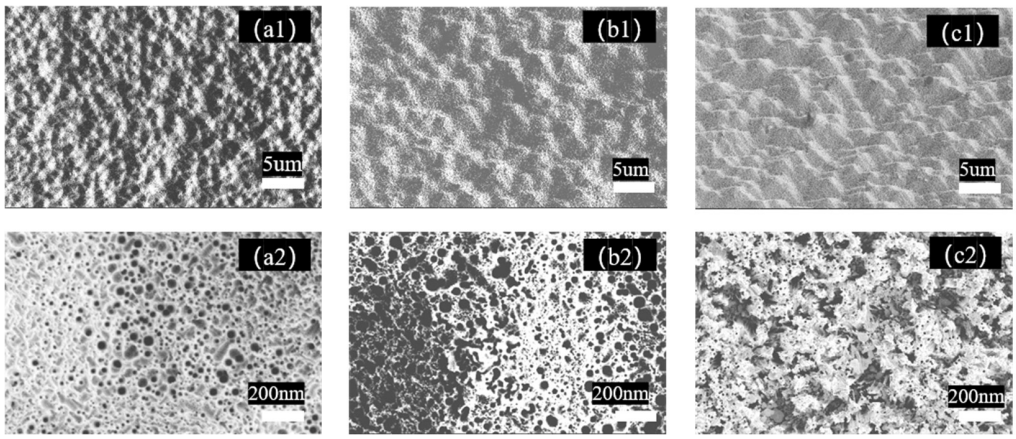

Figure 5. Relationship between the porous structure on the pyramids and the variation in $AgNO_3$ concentration. (**a1**) 0.03 Mol, (**b1**) 0.05 Mol, (**c1**) 0.06 Mol. (**a2**), (**b2**), and (**c2**) are the partially enlarged views of (**a1**), (**b1**), and (**c1**), respectively.

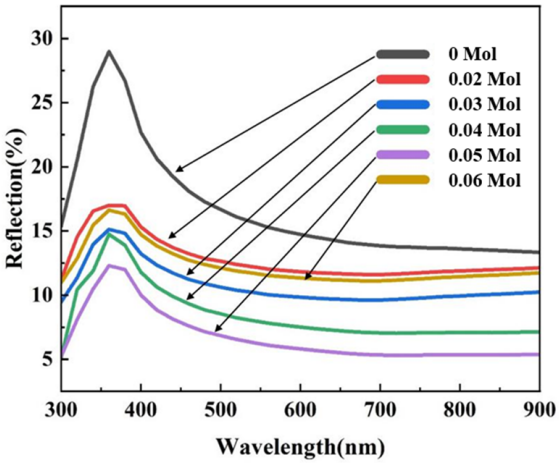

Figure 6. Relationship between the reflection spectrum of the silicon surface and the $AgNO_3$ concentration.

Subsequently, the pyramid/porous structures were transferred to the illuminated surface of the PSCs through a two-step nanoimprinting technique. In this step, the previously etched silicon sample can be utilized multiple times as an imprinting template. Figure 7 presents the transmittance of glass featuring different surface structures. It can be observed that the transmittance of flat glass is ~90%, while the transmittance of glass with pyramids and pyramid/porous structures is ~93% and ~95%, respectively. This outcome further demonstrates that due to the modulation imparted by the pyramid/porous design,

a greater number of photons are able to traverse through the glass and penetrate into the interior of the solar cell. Figure 8 presents the photovoltaic performance of cell devices with varying surface structures. The inset in Figure 8a shows surface photographs of cells with different structures. It can be observed that when the cell surface is unstructured (flat), the surface color appears lighter, with more prominent reflections visible. Upon introducing the pyramid structure, the surface color significantly darkens, indicating a reduction in optical reflection losses. The cell surface with the pyramid/porous structure exhibits the darkest color, suggesting minimal optical reflection losses, which is also corroborated by the reflection spectra of the three types of cells presented in Figure 8a.

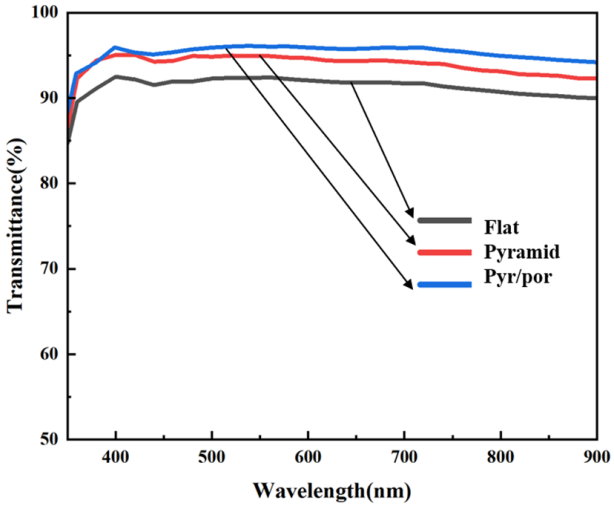

Figure 7. Transmittance of glass with different surface structures.

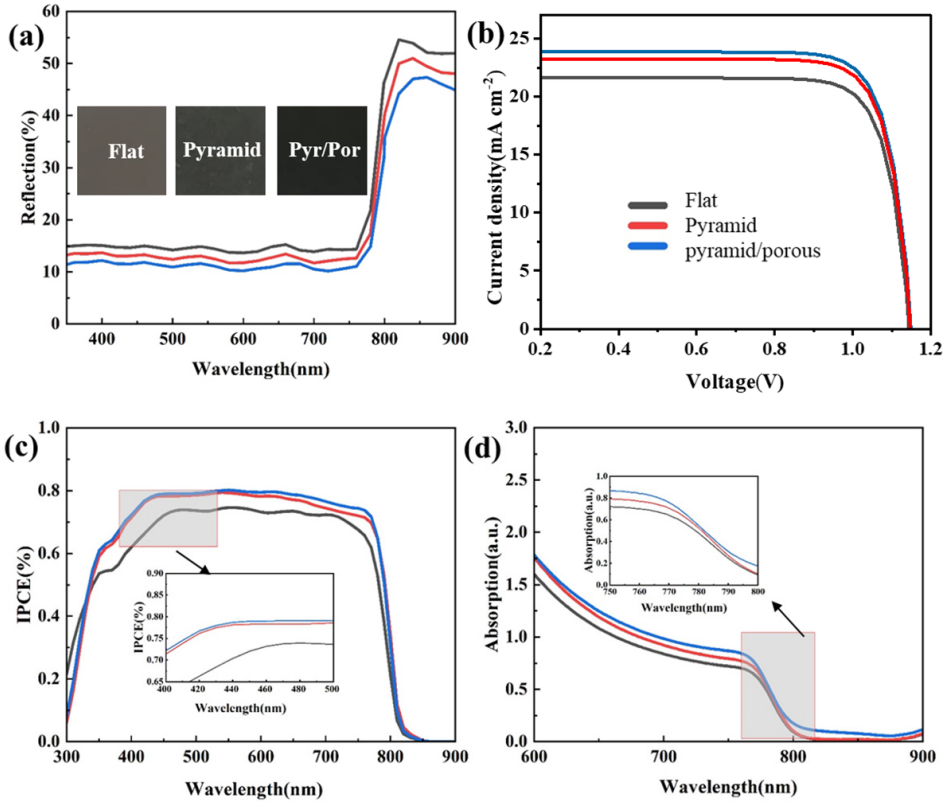

Figure 8. Optoelectronic performance of PSCs with different surface structures. (**a**) Surface reflection spectra, (**b**) current–voltage (I-V) characteristic curves, (**c**) external quantum efficiency (EQE), (**d**) absorption spectra. The inset in figure (**a**) shows photographs of devices with different surface structures.

Figures 8c and 8d, respectively, show the external quantum efficiency (EQE) and absorption spectrum of the cells. These figures reveal that, due to the reduction in reflection losses, the absorption spectrum of the corresponding cell is enhanced. The improved EQE also indicates that this additional light absorption is successfully converted into photocurrent. Figure 8b displays the current–voltage (I-V) characteristics of the tested cells for the three structures. It is evident that the introduction of structures significantly enhances the short-circuit current density (*J*sc) of the cells. The *J*sc values for the flat, pyramid, and pyramid/porous structures are 21.62, 23.24, and 23.86 mA/cm^2, respectively, as determined by averaging the results from 10 samples for each structure. In contrast, no significant differences were observed in the open-circuit voltage (*V*oc) and fill factor (FF) among the three cell types, with average values of ~1.15 V and ~83%, respectively. This is because the pyramid and porous structures are merely overlaid on the cell surface, modulating the incident light waves without altering the internal electrical structure of the cell. The PCEs of the three types of cells are 20.61%, 22.21%, and 22.78% in sequence. Compared to the unstructured surface, the introduction of the pyramid/porous structure results in a relative efficiency improvement of 9.5% for the cell.

4. Conclusions

In summary, this paper reports the fabrication of pyramid/porous composite structures on silicon surfaces through alkaline wet etching and metal-assisted chemical etching. Benefiting from the multiple refraction of incident light by the pyramids and the reduced refractive index mismatch between the pyramids and air due to the porous structure, this micro–nano composite structure exhibits significant advantages in suppressing surface optical reflection losses. Compared to planar silicon, the surface reflectivity of silicon with pyramid/porous structures decreases from 40.3% to 5.1%. Furthermore, the pyramid/porous structure was replicated onto the light-receiving surface of PSCs using nanoimprinting technology. With the modulation of the pyramid/porous structure, the response spectrum of the PSCs was improved. The photogenerated current density of the devices increased from 21.62 to 23.86 mA cm^2, with a relative enhancement in PCE of 9.5%. This structure is simple to fabricate and cost-effective, without compromising the electrical performance of the PSCs. Additionally, this structure can be readily replicated in large quantities and holds promise for optical enhancement in other similar optoelectronic devices.

Author Contributions: Conceptualization, B.L.; Methodology, Z.J. and Y.D.; Formal analysis, C.W.; Writing—original draft, X.S. (Xiaohao Shi); Writing—review & editing, X.W. and X.S. (Xiangqian Shen). All authors have read and agreed to the published version of the manuscript.

Funding: This research was funded by the Natural Science Foundation of Xinjiang Uygur Autonomous Region of China (Grant No. 2022D01C20) and the Tianshan Innovation Team Program of Xinjiang Uygur Autonomous Region of China (2023D14001).

Institutional Review Board Statement: Not applicable.

Informed Consent Statement: Not applicable.

Data Availability Statement: Data are contained within the article.

Conflicts of Interest: Author Xiaodan Wang was employed by the company Helmholtz-Zentrum Berlin für Materialien und Energie GmbH (HZB). The remaining authors declare that the research was conducted in the absence of any commercial or financial relationships that could be construed as a potential conflict of interest.

References

1. Liu, M.; John, M.B.; Snaith, H.J. Efficient planar heterojunction perovskite solar cells by vapour deposition. *Nature* **2013**, *501*, 395–398. [CrossRef] [PubMed]
2. Jin, Y.K.; Lee, J.W.; Jung, H.S.; Shin, H.; Park, N.G. High-efficiency perovskite solar cells. *Chem. Rev.* **2020**, *120*, 7867–7918.
3. Shen, X.; Lin, X.; Peng, Y.; Zhang, Y.; Long, F.; Han, Q.; Wang, Y.; Han, L. Two-Dimensional Materials for Highly Efficient and Stable Perovskite Solar Cells. *Nano-Micro Lett.* **2024**, *16*, 201. [CrossRef] [PubMed]
4. Li, N.X.; Niu, X.X.; Chen, Q.; Zhou, H. Towards commercialization: The operational stability of perovskite solar cells. *Chem. Soc. Rev.* **2020**, *49*, 8235–8286. [CrossRef] [PubMed]
5. Xu, C.Y.; Hu, W.; Wang, G.; Niu, L.; Elseman, A.M.; Liao, L.; Yao, Y.; Xu, G.; Luo, L.; Liu, D.; et al. Coordinated Optical Matching of a Texture Interface Made from Demixing Blended Polymers for High-Performance Inverted Perovskite Solar Cells. *ACS Nano* **2020**, *14*, 196–203. [CrossRef]
6. NREL—The National Renewable Energy Laboratory. Best Research-Cell Efficiency Chart. Version 2024. Available online: www.nrel.gov/pv/cell-efficiency.html (accessed on 1 June 2024).
7. Park, J.; Kim, J.; Yun, H.S.; Paik, M.J.; Noh, E.; Mun, H.J.; Kim, M.G.; Shin, T.J.; Seok, S.I. Controlled growth of perovskite layers with volatile alkylammonium chlorides. *Nature* **2023**, *616*, 724–730. [CrossRef]
8. Green, M.A.; Dunlop, E.D.; Siefer, G.; Yoshita, M.; Kopidakis, N.; Bothe, K.; Hao, X. Solar cell efficiency tables (version 61). *Prog. Photovolt.* **2023**, *31*, 3–16. [CrossRef]
9. Wang, J.; Luo, S.; Lin, Y.; Chen, Y.; Deng, Y.; Li, Z.; Meng, K.; Chen, G.; Huang, T.; Xiao, S.; et al. Templated growth of oriented layered hybrid perovskites on 3D-like perovskites. *Nat. Commun.* **2020**, *11*, 582. [CrossRef]
10. He, L.; Su, H.Z.; Li, Z.P.; Liu, H.; Shen, W.Z. Multiple Function Synchronous Optimization by PbS Quantum Dots for Highly Stable Planar Perovskite Solar Cells with Efficiency Exceeding 23%. *Adv. Funct. Mater.* **2023**, *33*, 2213963. [CrossRef]
11. Chen, C.; Zheng, S.; Song, H. Photon management to reduce energy loss in perovskite solar cells. *Chem. Soc. Rev.* **2021**, *50*, 7250–7329. [CrossRef]
12. Zhao, S.; Zhou, H.; Wang, S.Y.; Han, F.; Jiang, S.-H.; Shen, X.-Q. Design of high efficiency perovskite-silicon tandem solar cells based on plasmonic enhancement of metal nanosphere. *Acta Phys. Sin.* **2022**, *71*, 038801. [CrossRef]
13. Raut, H.K.; Ganesh, V.A.; Nair, A.S.; Ramakrishna, S. Anti-reflective coatings: A critical, in-depth review. *Energy Environ. Sci.* **2011**, *4*, 3779–3804. [CrossRef]
14. Yu, P.; Wu, J.; Liu, S.; Xiong, J.; Jagadish, C.; Wang, Z.M. Design and fabrication of silicon nanowires towards efficient solar cells. *Nano Today* **2016**, *11*, 704–737. [CrossRef]
15. Dudem, B.; Heo, J.H.; Leem, J.W.; Yu, J.S.; Im, S.H. $CH_3NH_3PbI_3$ planar perovskite solar cells with antireflection and self-cleaning function layers. *J. Mater. Chem. A* **2016**, *4*, 7573–7579. [CrossRef]
16. Peer, A.; Bi, R.; Park, J.; Shinar, R.; Shinar, J. Light management in perovskite solar cells and organic LEDs with microlens arrays. *Opt. Express* **2017**, *25*, 10704–10709. [CrossRef]
17. Choi, J.S.; Jang, Y.W.; Kim, U.; Choi, M.; Kang, S.M. Optically and mechanically engineered anti-reflective film for highly efficient rigid and flexible perovskite solar cells. *Adv. Energy Mater.* **2022**, *12*, 2201520. [CrossRef]
18. Al-Husseini, A.M.; Lahlouh, B. Influence of pyramid size on reflectivity of silicon surfaces textured using an al-alkaline etchant. *Bull. Mater. Sci.* **2019**, *42*, 152. [CrossRef]
19. Cao, Y.; Liu, A.; Li, H.; Liu, Y.; Qiao, F.; Hu, Z.; Sang, Y. Fabrication of silicon wafer with ultra-low reflectance by chemical etching method. *Appl. Surf. Sci.* **2011**, *257*, 7411–7414. [CrossRef]
20. Krajewski, M.; Callies, A.; Heydarian, M.; Heydarian, M.; Hanser, M.; Schulze, P.S.C.; Bläsi, B.; Höhn, O. Roller nanoimprinted honeycomb texture as an efficient antireflective coating for perovskite solar cells. *Adv. Mater. Interfaces* **2023**, *10*, 2300134. [CrossRef]
21. Schmager, R.; Hossain, I.M.; Schackmar, F.; Richards, B.S.; Gomard, G.; Paetzold, U.W. Light coupling to quasi-guided modes in nanoimprinted perovskite solar cells. *Sol. Energy Mater. Sol. Cells* **2019**, *201*, 110080. [CrossRef]
22. Zhang, Z.; Xu, Z.M.; Sun, T.Y.; He, J.; Xu, H.F.; Zhang, X.M.; Liu, S.Y. The fabrication of the antireflective periodic nano-arrary structure on Si surface using nanoimprint lithography and the study on its properties. *Acta Phys. Sin.* **2013**, *62*, 168102. [CrossRef]